INORGANIC CHEMISTRY FRONTIERS

RESEARCH ARTICLE

View Article Online
View Journal | View Issue

Cite this: *Inorg. Chem. Front.*, 2023, **10**, 7167

Efficient triplet energy transfer in a 0D metal halide hybrid with long persistence room temperature phosphorescence for time-resolved anti-counterfeiting†

Jie Li,‡[a] Jingjie Wu,‡[b] Yonghong Xiao,[a] Longshi Rao,[c] Ruosheng Zeng,*[d] Ke Xu,[e] Xiao-Chun Huang,[a] Jin Z. Zhang[f] and Binbin Luo*[a]

Endowing metal halide hybrids (MHHs) with time-resolved emission and afterglow could significantly broaden their applications in fields such as information security and anti-counterfeiting. Nonetheless, there have been relatively few successes in developing organic cations with persistent room-temperature phosphorescence (RTP) to construct MHHs with afterglow. In this work, we synthesize a new polyazole, 3,5-di(1*H*-pyrazol-4-yl)-4*H*-1,2,4-triazol-4-amine (DPTA), with green persistent RTP up to 1.5 s. The afterglow of DPTA reaches up to ~1.0 s even after being assembled into 0D $(DPTAH_3)InCl_6{\cdot}2.5H_2O$ (DIC). Due to strong overlap between the triplet emission of DPTA and $^1S_0 \rightarrow {}^3P_x$ absorption of Sb^{3+}, efficient triplet energy transfer (TET) with the highest yield of 65.3% and a near-unity photoluminescence quantum yield (PLQY) is achieved. More importantly, the afterglow persistence time of DIC:*x*% Sb can be easily tailored through Sb^{3+} doping. Given the Sb^{3+}-dependent emission color and long persistence time, a series of DIC:*x*% Sb are successfully utilized to demonstrate high-security-level anti-counterfeiting application. This work shows an effective strategy for designing new MHHs with tunable emission and afterglow persistence time.

Received 3rd September 2023,
Accepted 23rd October 2023

DOI: 10.1039/d3qi01774e

rsc.li/frontiers-inorganic

1. Introduction

Zero-dimensional (0D) metal halide hybrids (MHHs) with fully isolated organic cations and metal halide polyhedra have kindled tremendous interest in solid-state emission, X-ray scintillators, photoluminescence (PL) sensing, anti-counterfeiting, *etc.*[1–8] Similar to halide perovskites,[9–15] the photophysical properties of MHHs are mainly determined by the metal and halide components, while the organic component mainly serves as a structural counterion.[16–19] To modulate the optical properties of MHHs, various strategies, such as adopting diverse organic cations[20–23] and doping metal ions,[24–30] have been utilized. Compared to inorganic ions with limited choice and coordinated environments, organic components offer more flexibility in structural manipulation and regulation of optical properties.[31] Therefore, there has been strong interest in developing new organic cations with unique optical characteristics and enhanced interaction with inorganic emissive centers to improve the optical properties of MHHs for different applications.[32–34]

Conjugated organic molecules with persistent room-temperature phosphorescence (RTP) are highly attractive in bioimaging, chemical sensing and anti-counterfeiting.[31] To date, only a few organic counter-cations such as tetraphenylphosphonium and triphenylsulphonium have been successfully assembled into low-dimensional MHHs with RTP.[35–40] The persistent RTP of most A-site organic cations is usually absent once they are integrated with an emissive metal halide polyhedron due to their large free volume of organic cations in

[a]*Department of Chemistry and Chemical Engineering, Key Laboratory for Preparation and Application of Ordered Structural Materials of Guangdong Province, Shantou University, Shantou, 515063, P. R. China. E-mail: bbluo@stu.edu.cn*
[b]*Chaozhou Branch of Chemistry and Chemical Engineering Guangdong Laboratory, Chaozhou 521000, P. R. China*
[c]*Department of Mechanical Engineering, College of Engineering, Shantou University, Shantou 515063, P. R. China*
[d]*School of Physical Science and Technology, State Key Laboratory of Featured Metal Materials and Life-Cycle Safety for Composite Structures, Guangxi University, Nanning 530004, P. R. China*
[e]*Multiscale Crystal Materials Research Center, Shenzhen Institute of Advanced Technology, Chinese Academy of Sciences, Shenzhen 518055, P. R. China*
[f]*Department of Chemistry and Biochemistry, University of California, Santa Cruz, California 95064, USA*

†Electronic supplementary information (ESI) available: Experimental methods, crystal structures and data, EDS mapping, NMR, ICP-AES, PL, delayed PL and PLE spectra, fitting results of the PL lifetime, PLQY test. CCDC 2282720 (DIC) and 2282721 (DPTA). For ESI and crystallographic data in CIF or other electronic format see DOI: https://doi.org/10.1039/d3qi01774e

‡These authors contributed equally to this work.

hybrids.[35] Therefore, it still remains a great challenge to acquire MHHs with persistent RTP.

In this work, we have successfully synthesized a nitrogen-rich heterocycle 3,5-di(1*H*-pyrazol-4-yl)-4*H*-1,2,4-triazol-4-amine (DPTA), which exhibits persistent RTP up to 1.5 s. Due to the multiple protonated sites and strong coulombic interaction with metal halide polyhedra, the rotation and vibration of DPTA are greatly suppressed. Long afterglow remains even after being assembled into 0D $(DPTAH_3)InCl_6{\cdot}2.5H_2O$ (DIC). Moreover, efficient triplet energy transfer (TET) is achieved *via* Sb^{3+} doping that leads to unique Sb^{3+}-dependent RTP lifetimes and emission colors.

2. Results and discussion

2.1 Structural and optical properties of DPTA

DPTA was synthesized through a simple solvothermal method (Fig. 1a) with the detailed synthetic procedure given in the ESI.† Single-crystal X-ray diffraction (SCXRD) studies show that DPTA adopts a monoclinic *Cc* space group and the detailed crystal parameters are given in Table S1.† Due to the presence of electronegative N atoms in DPTA, an intermolecular hydrogen-bonding network with bond lengths (H···N) ranging from 2.02 to 2.26 Å is constructed (Fig. 1b and Fig. S1a†), which suppresses the vibration and rotation of DPTA molecules. DPTA molecules are parallelly arranged through π–π stacking with an intermolecular spacing around 3.545 Å (Fig. S1b†). The well-matched powder XRD with the simulated pattern (Fig. 1c) and the ^{1}H nuclear magnetic resonance (^{1}H-NMR) spectrum (Fig. S2†) indicate the high purity of DPTA.

Fig. 2 shows the UV-vis absorption and prompt PL spectra of DPTA powders and solution. From the electronic absorption spectrum in Fig. 2a, it can be seen that DPTA exhibits gradually increased absorption towards shorter wavelengths with two step-like onsets starting from 380 and 320 nm, respectively. Upon excitation at optimal 385 nm, the white DPTA powders show a cyan emission located at 455 nm with a PL quantum yield (QY) of 10.4%, as shown in Fig. 2a. The corresponding PL excitation (PLE) spectrum of DPTA powders shows a main band that peaked at 385 nm with a distinct shoulder at 320 nm upon monitoring at 455 nm, which correlates well with the absorption spectrum. Interestingly, DPTA powders exhibit excitation-dependent PL, as shown in Fig. S3.† The main peak shifts from 383 to 460 nm gradually upon excitation at different wavelengths. This excitation-dependent PL is usually found in pyrazole derivatives due to the excited-state inter/intra-molecular proton transfer.[41,42]

When dissolving DPTA in dimethyl sulphoxide (DMSO), the absorption spectrum of DPTA solution resembles that in the powder form, except the disappearance of the absorptive band around 365 nm (Fig. 2b), which is attributed to DPTA in the aggregated form. Interestingly, the PL spectrum of DPTA solution shows two highly overlapped bands upon 365 nm excitation, which are centered at 425 and 441 nm, respectively. Nevertheless, the emission blue-shifts to 395 nm upon excitation at 320 nm, confirming the presence of multiple emissive excited states in DPTA.

Fig. 2c shows the delayed PL of DPTA at 1 ms upon photoexcitation at 385 nm, in which a major PL band that peaked at 476 nm is observed along with two distinct shoulders at 435 and 518 nm. Because of the presence of a high percentage of heteroatoms and strong intermolecular interaction, the triplet emission of DPTA likely results from the n–π* electronic transition.[43] Compared to the prompt PL spectrum of DPTA powders, the main delayed PL band red-shifts by ~20 nm,

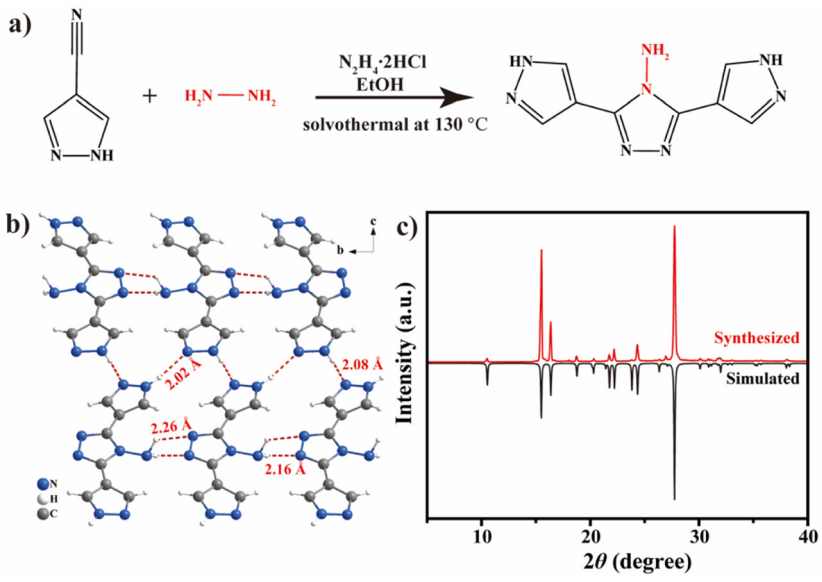

Fig. 1 (a) Reaction pathway, (b) crystal structure and (c) XRD pattern of DPTA. The red dashed lines in (b) indicate the intermolecular hydrogen bonds.

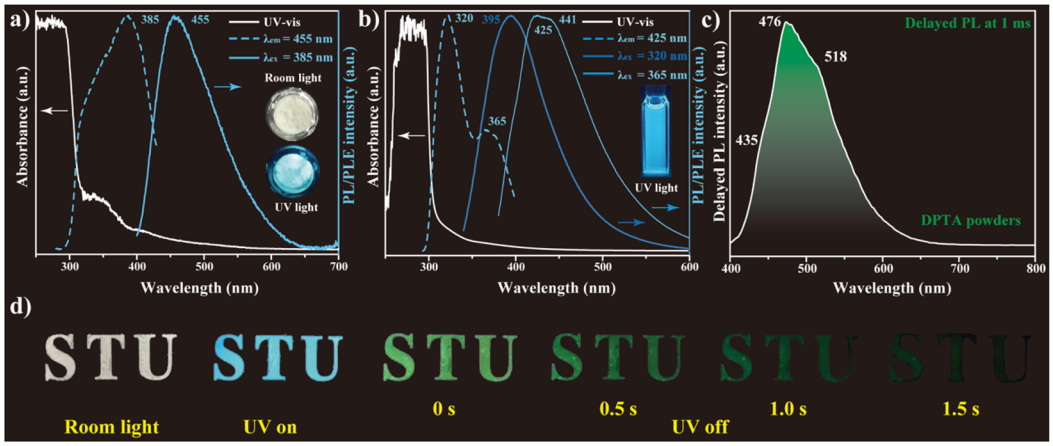

Fig. 2 UV-vis absorption, prompt PL (solid line) and PLE (dashed line) spectra of (a) DPTA powders and (b) 0.1 M DPTA solution (solvent: DMSO). (c) Delayed PL (λ_{ex} = 385 nm) of DPTA powders at 1 ms. (d) Digital pictures of the "STU" pattern filled with DPTA powders under natural light and UV irradiation and with the UV irradiation switched off. The afterglow pictures were taken using Huawei P60 Pro.

which is attributed to the internal conversion (IC) and intersystem crossing (ISC) from the singlet states to the triplet states. Consistent with the prompt and delayed PL spectrum, the "STU" pattern filled with DPTA powders exhibits cyan emission under UV irradiation (365 nm), while a green afterglow up to 1.5 s emerges once the UV irradiation is switched off (Fig. 2d). The lifetime of this persistent RTP is further confirmed through time-resolved PL, in which the lifetime achieved is as long as 590 ms (Fig. S4†).

2.2 Structural and optical properties of DIC

Protonated DPTA ($[DPTAH_3]^{3+}$) was further hybridized with indium chloride and the structure of DIC is shown in Fig. 3a and b. The colorless DIC single crystal possesses a triclinic $P\bar{1}$ space group (Table S2†) with the chemical formula $(DPTAH_3)InCl_6{\cdot}2.5H_2O$. Similar to other 0D metal-based MHHs,[11,20,44] $[DPTAH_3]^{3+}$ mainly interacts with $[InCl_6]^{3-}$ octahedra through coulombic and hydrogen-bonding interaction. Apart from the strong π–π stacking interaction (3.402 Å) between adjacent $[DPTAH_3]^{3+}$ (Fig. 3b), the hydrogen-bonding network mediated by the H_2O guest is further constructed in DIC (Fig. S5†). Therefore, $[DPTAH_3]^{3+}$ cations are fixed in a relatively rigid environment, which effectively hinders the molecular vibration and rotation. The good agreement between the XRD pattern of DIC measured (Fig. 3c) and the simulated result indicates the high purity of the prepared sample.

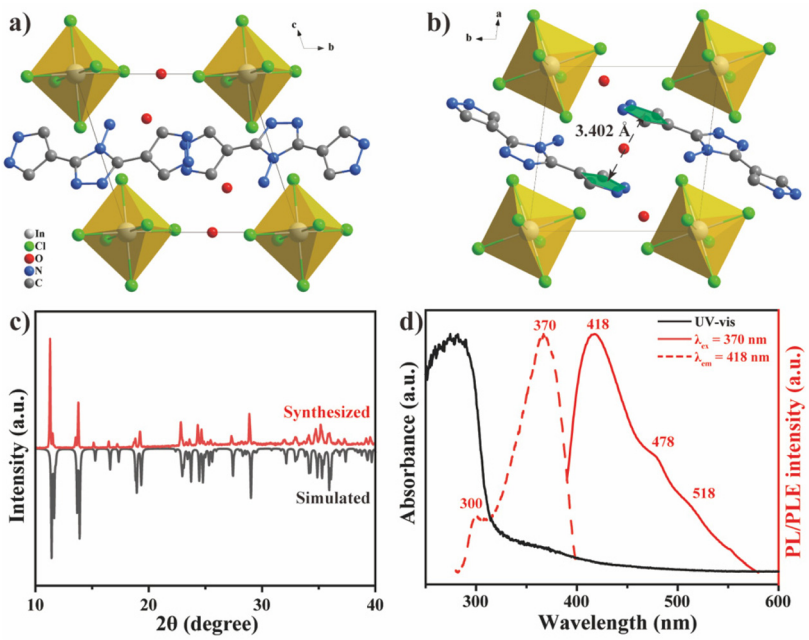

Fig. 3 Unit cell of DIC viewed from (a) *a* and (b) *c* axes; H atoms are omitted. (c) XRD pattern of DIC. (d) UV-vis, PL and PLE spectra of DIC.

Similar to DPTA, DIC also shows a sharp absorption onset around 320 nm (Fig. 3d), indicating the predominant contribution of DPTA to the band edge of DIC. The main emission peak of DIC blue-shifts to 418 nm with two distinct shoulders located at 478 and 518 nm in the prompt PL spectrum, in good agreement with the delayed PL spectrum of DPTA (Fig. 2c). Such a coincidence implies the boosted RTP of DPTA after hybridization with metal halides, possibly arising from the rigid structural environment and external heavy-atom effects of DIC. Correspondingly, the PLE spectrum shows a main band that peaked around 370 nm with a small shoulder at 300 nm, agreeing well with that of DPTA solution, indicating the dominant contribution of DPTA to the optical properties of DIC. Similarly, excitation-dependent PL is also observed for DIC (Fig. S6†), which is attributed to the excited-state intermolecular proton transfer. Additionally, DIC shows good stability in open air, as shown in Fig. S7,† in which no distinct peaks of impurities are observed after 72 h.

2.3 Optical properties of Sb^{3+}-doped DIC

Sb^{3+} was introduced into DIC as a dopant with different doping levels (abbreviated as DIC:*x*% Sb, where *x*% represents the molar feed ratio). The XRD patterns of DIC:*x*% Sb coincide well with those of pristine DIC, indicating the absence of new phases after doping (Fig. S8a†). However, no notable shift of diffraction peaks is observed for DIC:*x*% Sb, which is possibly attributed to the similar ionic radii of Sb^{3+} (0.76 Å, CN = 6) and In^{3+} (0.80 Å, CN = 6). To validate the successful doping of Sb^{3+}, energy dispersive spectroscopy (EDS) was conducted, as shown in Fig. S8b.† DIC:10% Sb shows a uniform distribution of each element, confirming the homogeneous doping of Sb^{3+}. The real doping concentration was further determined through inductively coupled plasma atomic emission spectroscopy (ICP-AES), as shown in Table S3.†

Fig. 4a shows the UV-vis diffuse reflectance spectra of DIC:*x* % Sb. Compared to pristine DIC, a new absorption band that peaked at 380 nm with a weak tail extending to ~500 nm is observed for Sb^{3+}-doped DIC. This absorption band becomes more prominent concurrent with the appearance of a new band that peaked at 294 nm once the doping level of Sb^{3+} is increased to 20%. Consistent with previously reported Sb^{3+}-doped MHHs,[11,26,28,45] doping with Sb^{3+} often results in new optical properties for hosts without ns^2 metal ions, since the s-electrons of the Sb^{3+} dopant could create energy levels within the bandgap of the host, thereby generating new absorption bands at longer wavelengths.[29,45,46] According to previous works,[4,28] these two bands at 294 and 380 nm are assigned to the characteristic $^1S_0$ to $^1P_1$ and ^3P_x transitions of Sb^{3+}, respectively.

Correspondingly, all Sb^{3+}-doped DIC samples exhibit an Sb^{3+}-specific broadband emission that peaked at 580 nm in the PL spectra (Fig. 4b), which is absent for undoped DIC.

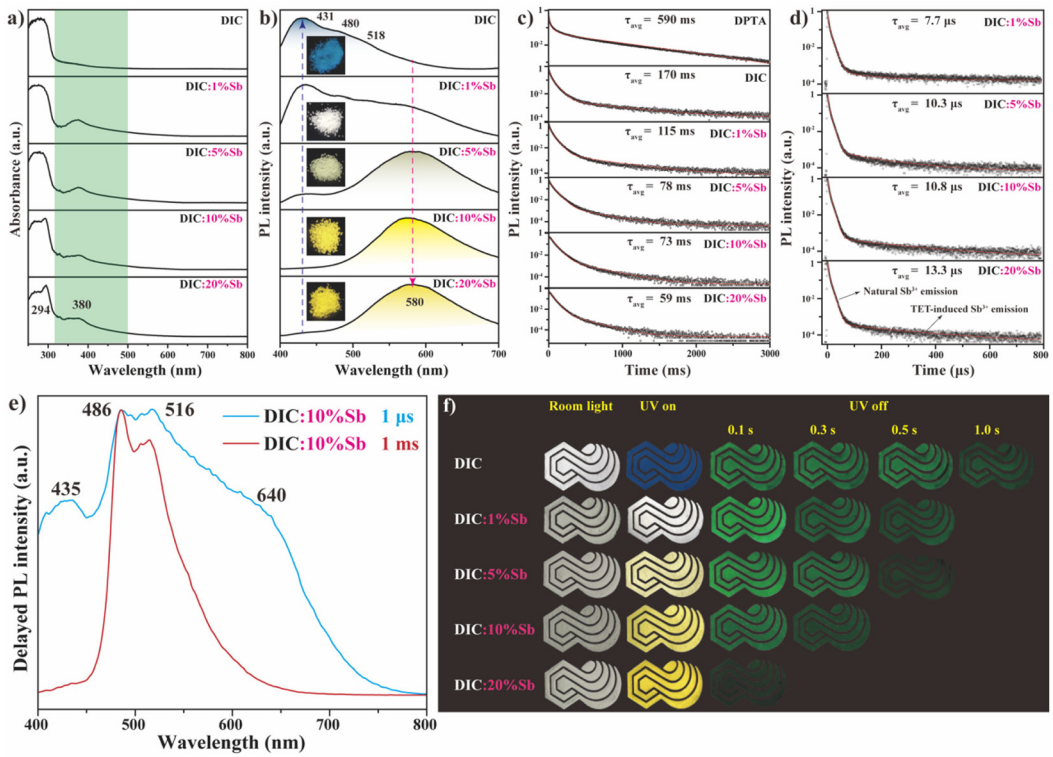

Fig. 4 (a) UV-vis diffuse reflectance spectra and (b) PL spectra of DIC:*x*% Sb. (c) TRPL of DIC:*x*% Sb at (c) 518 nm (λ_{ex} = 365 nm) and (d) 580 nm (λ_{ex} = 365 nm). (e) Delayed PL spectra of DIC:10% Sb at 1 μs and 1 ms. (f) Digital pictures of the "∞/CO" pattern filled with DIC:*x*% Sb powders under natural room light and UV irradiation and with the UV irradiation switched off.

Upon increasing the doping level, the intensity of Sb^{3+} emission increases dramatically along with the reduction of emission intensity from DPTA, indicating possible energy transfer from DPTA to Sb^{3+}. Moreover, the PLQY can reach up to near-unity for DIC:10% Sb, while further increasing the doping level (DIC:20% Sb) results in a decrease of the PLQY (Fig. S9†), possibly due to concentration quenching. By tuning the doping level of Sb^{3+}, various emission colors from blue to white and yellow can be readily achieved. The PLE spectra of DIC:*x*% Sb monitored at 580 nm are shown in Fig. S10,† where a major band (~338 nm) along with a gradually increasing shoulder (~363 nm) is found once the doping level of Sb^{3+} is increased. The main peak at 338 nm, not observed in the PLE of pure DIC, is assigned to the electronic transition of $^1S_0$ to ^3P_x for Sb^{3+},[5] while the 363 nm peak coincides well with the PLE of DPTA solution and DIC (Fig. 2b). In view of the isolated $[DPTAH_3]^{3+}$ in DIC, the optical properties of $[DPTAH_3]^{3+}$ are expected to resemble those of DPTA solution. As a result, the 363 nm peak in the PLE spectrum is attributed to the efficient TET from $[DPTAH_3]^{3+}$ to the Sb^{3+} dopant.

To better understand the TET process, time-resolved PL (TRPL) was conducted, with results shown in Fig. 4c. All TRPL decay profiles of DPTA and DIC:*x*% Sb at 518 nm are fitted with a triple-exponential function, with the fitting parameters summarized in Table S4.† DPTA shows an average lifetime up to 590 ms, consistent with the observed long afterglow around 1.5 s. Upon being assembled into rigid DIC, the average lifetime of DPTA decreases to 170 ms, due to the enhanced ISC process induced by the external heavy atom effect. Furthermore, the average lifetime decreases dramatically to 59 ms once the feed doping level of Sb^{3+} is increased to 20%. The TET yield is calculated according to the following equation:[47]

$$\Phi_{TET} = 1 - \frac{\tau_{avg}}{\tau_{DIC}}$$

where Φ_{TET} is the TET yield and τ_{avg} and τ_{DIC} are the average lifetimes of DIC:*x*% Sb and pristine DIC, respectively. The TET yields for DIC:*x*% Sb are given in Table S4,† wherein the highest value of 65.3% is achieved for DIC:20% Sb. In contrast, DIC:*x*% Sb exhibit increased average lifetimes of Sb^{3+} emission from 7.7 μs for DIC:1% Sb to 13.3 μs for DIC:20% Sb (Fig. 4d). Two short lifetimes around several microseconds and a long lifetime up to hundreds of microsecond are found through fitting the decay profiles (Table S5†). The two short lifetimes are assigned to the characteristic Sb^{3+} emission, while the longest one is attributed to TET-induced Sb^{3+} emission. The changes in PL intensity and lifetime further support our hypothesis that TET happens between organic DPTA and the inorganic Sb^{3+} dopant.

The TET from DPTA to Sb^{3+} is further substantiated from the delayed PL spectrum. As shown in Fig. 4e, the delayed PL of DIC:10% Sb at 1 μs shows a broadband emission spanning the whole visible range with four distinct bands that peaked at 434, 485, 516 and 640 nm, which agrees well with the prompt PL of pristine DIC (Fig. 4b), except for the shoulder at 640 nm. Intriguingly, both the peak at 435 nm and the shoulder at 640 nm are absent in the delayed PL of DIC:10% Sb at 1 ms, indicating that their lifetimes are shorter than 1 ms. Considering the fact that the characteristic Sb^{3+} emission usually occurs at ~600 nm with a lifetime of around several microseconds,[11,44,45] we attribute the 640 nm peak to the Sb^{3+} emissive center. In contrast to the complete quenching at 435 nm in the delayed PL of DIC:10% Sb at 1 ms, this peak is clearly observed in the delayed PL of pristine DPTA at 1 ms (Fig. 2c). Since the triplet emission at 435 nm overlaps with the absorption of Sb^{3+} (Fig. S11†), this band may be quenched *via* Förster resonance energy transfer (FRET) once the Sb^{3+} dopant is introduced into DIC.

Although the emission color of DIC:*x*% Sb changes from blue to white and yellow under UV irradiation (Fig. 4f), all the prepared hybrids show a green afterglow once the UV irradiation is switched off, which is from the persistent RTP of DPTA. However, the afterglow lifetime of the "∞/CO" pattern decreases gradually from 1.0 s for DIC to 0.1 s for DIC:20% Sb, arising from the efficient TET that results in the Sb^{3+}-dependent afterglow time of DIC:*x*% Sb.

A temperature-dependent PL study was conducted to gain further insight into the TET process. Upon lowering the temperature, five notable emission bands located at 430, 463, 478, 499 and 518 nm are observed, as shown in Fig. S12a.† Nevertheless, DIC:10% Sb exhibits a totally different behavior, as shown in Fig. S12b.† Two peaks assigned to emissive centers of DPTA (435 nm) and the Sb^{3+} dopant (580 nm) are clearly observed. The intensity of the Sb^{3+} emission decreases monotonously upon lowering the temperature from 325 to 200 K and then increases with the reduction of the temperature from 200 to 77 K. In contrast, the emission of DPTA at 435 nm shows a different dependence in the temperature range of 325–77 K, where the emission intensity increases first followed by reduction, validating the competitive relation between DPTA and Sb^{3+} emission.

2.4 DFT calculations of Sb^{3+}-doped DIC

Density functional theory (DFT) calculations (Fig. 5) were conducted to better understand the effect of Sb^{3+} doping on the electronic structures of the host. Pristine DIC shows a direct bandgap (Fig. 5a) of ~2.79 eV, smaller than that calculated from the UV-vis spectrum due to the well-known underestimated bandgap error for the Perdew–Burke–Ernzerhof (PBE) exchange–correlation functional. Different from that the band edge of low-dimensional MHHs usually derives from the metal halide polyhedra,[11,44] the flat valence band maxima (VBM) of DIC are mainly composed of Cl-p and N-p (Fig. 5b), while the conduction band minima (CBM) are derived from DPTA according to the projected density of states (PDOS). Upon introducing Sb^{3+} dopants into DIC, the value of the bandgap decreases slightly to 2.61 eV (Fig. 5c), an energy level contributed from Sb $5s^2$ is created within the bandgap, consistent with the previous results.[11,29] Similarly, the orbital components of the band edge are mainly contributed by DPTA (Fig. 5d). The dominant contribution of DPTA to the CBM and VBM of DIC

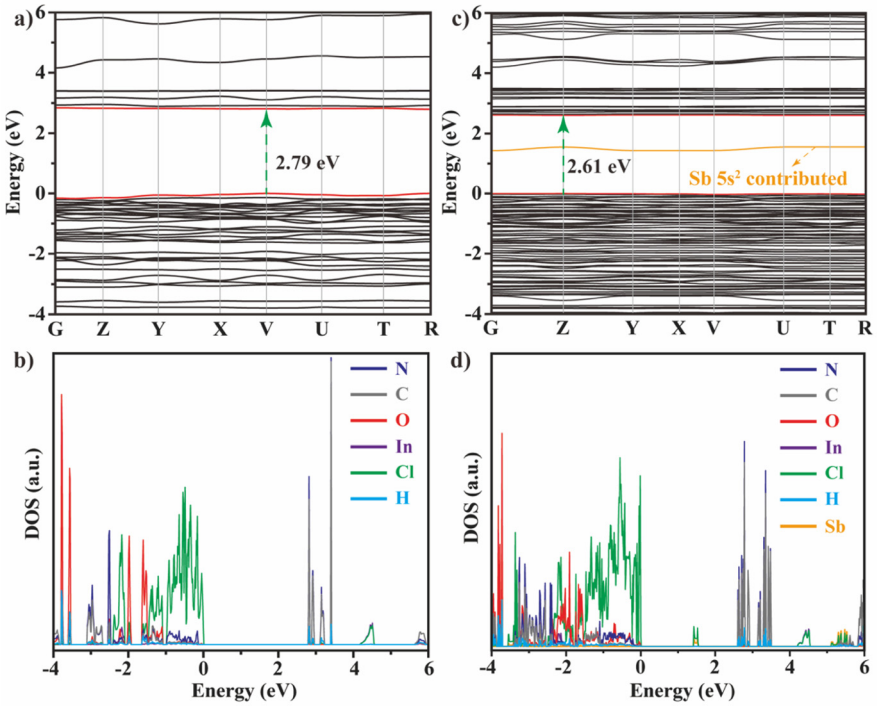

Fig. 5 Band structures and calculated PDOS of DIC (a and b) and Sb-doped DIC (c and d).

agrees well with the experimental results that the optical properties of DIC mainly derive from DPTA.

2.5 TET mechanism of Sb^{3+}-doped DIC

Based on the above experimental results, a TET mechanism is proposed and schematically shown in Fig. 6. Upon excitation at 365 nm, electrons in the ground state (S_0) of DPTA are promoted to the first excited singlet state (S_1). Subsequently, some excited electrons relax back to the ground electronic states while other electrons undergo an ISC process to the triplet states (T_n). The recombination of triplet excitons results in broadband RTP in the 400 to 650 nm region, which overlaps with the electronic transition of $^1S_0 \rightarrow {}^3P_x$ for Sb^{3+}. Therefore, TET will occur *via* the FRET mechanism upon the introduction of the Sb^{3+} dopant.

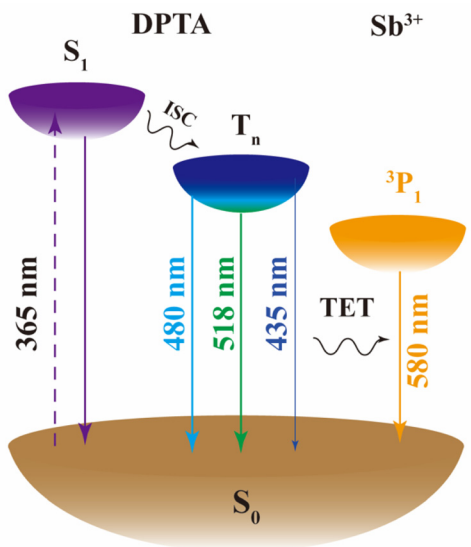

Fig. 6 Schematic illustration of the TET mechanism in DIC:*x*% Sb.

2.6 Anti-counterfeiting applications of DIC:*x*% Sb

To take advantage of the Sb^{3+}-dependent afterglow lifetime of DIC:*x*% Sb, a proof-of-concept for time-resolved information encryption was conducted, as shown in Fig. 7. DIC:*x*% Sb and non-emissive KBr were filled into the 888-shaped pattern (Fig. 7a). Although an identical optical appearance of "888" under natural room light was observed, this pattern shows a distinct "L88" with yellow emission under UV light. Upon removing 365 nm UV light, the letters "LUO" with green afterglow are found. In principle, the information can be multiply encrypted through combining DIC:*x*% Sb samples with a customized afterglow lifetime. Similarly, the time-dependent emission feature of DIC:*x*% Sb exhibits great potential in anti-counterfeiting, as shown in Fig. 7b. The logo of Shantou University made with DIC:*x*% Sb shows a phoenix (filled with DIC:10% Sb) on the top of a cloud (filled with DIC). Under the excitation of 365 nm UV light, the logo shows a golden phoenix with a blue cloud. Due to the similar afterglow color of DIC and DIC:10% Sb, a complete green logo is observed at the delay time of 0.1 s. However, the golden phoenix disappears while the green cloud remains after 0.5 s due to the short afterglow lifetime of DIC:10% Sb. These results demon-

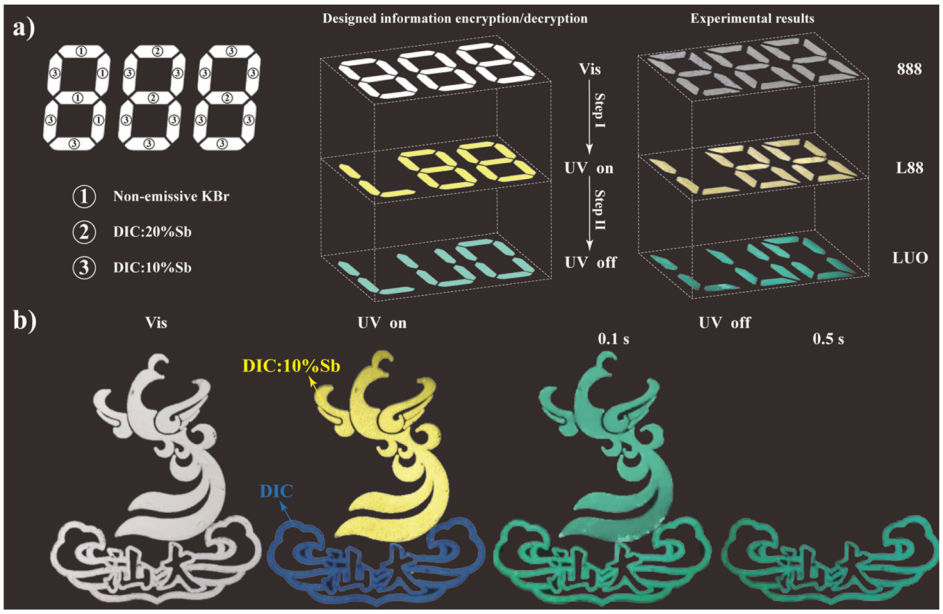

Fig. 7 (a) Schematic illustration of the information encryption and decryption of "888" based on DIC:*x*% Sb. (b) Time-resolved anti-counterfeiting of the Shantou University logo made with DIC:*x*% Sb.

strate the great potential of DIC:*x*% Sb for applications in high-security-level anti-counterfeiting.

3. Conclusion

In summary, we have synthesized a new polyazole heterocycle DPTA with green persistent RTP up to 1.5 s. The afterglow of DPTA persists even after being hybridized with indium halide. Comprehensive photophysical studies reveal that efficient TET from DPTA to the Sb^{3+} dopant happens *via* a FRET mechanism, resulting in various emission colors and afterglow times of DIC:*x*% Sb. Benefiting from the Sb^{3+}-dependent emission colors and afterglow lifetimes, DIC:*x*% Sb demonstrate good potential in time-resolved anti-counterfeiting and information security applications. This work provides new insights into the photophysical properties of MHHs with persistent RTP for high-security-level anti-counterfeiting.

Author contributions

Jie Li: methodology, investigation, and editing; Jingjie Wu: data curation and investigation; Yonghong Xiao: investigation; Longshi Rao: investigation; Ruosheng Zeng: investigation, characterization, and supervision; Ke Xu: resources; Xiao-Chun Huang: supervision; Jin Z. Zhang: supervision; Binbin Luo: supervision, project administration, and funding acquisition.

Conflicts of interest

The authors declare no competing financial interest.

Acknowledgements

This project was supported by the Guangdong Basic and Applied Basic Research Foundation (2022A1515011997), the Li Ka Shing Foundation Cross-Disciplinary Research Project (2020LKSFG09A), and the Open Foundation of Guangxi Key Laboratory of Processing for Nonferrous Metals and Featured Materials (2022GXYSOF14). K. X. is thankful for the financial support from the National Natural Science Foundation of China (52203343) and the Shenzhen Science and Technology Program (20210607151625001).

References

1 M. Li and Z. Xia, Recent Progress of Zero-Dimensional Luminescent Metal Halides, *Chem. Soc. Rev.*, 2021, **50**, 2626–2662.
2 G. Zhou, B. Su, J. Huang, Q. Zhang and Z. Xia, Broad-Band Emission in Metal Halide Perovskites: Mechanism, Materials, and Applications, *Mater. Sci. Eng., R*, 2020, **141**, 100548.
3 L. Zhou, J. F. Liao and D. B. Kuang, An Overview for Zero-Dimensional Broadband Emissive Metal-Halide Single Crystals, *Adv. Opt. Mater.*, 2021, **9**, 2100511.
4 Y. Jing, Y. Liu, M. Li and Z. Xia, Photoluminescence of Singlet/Triplet Self-Trapped Excitons in Sb^{3+}-Based Metal Halides, *Adv. Opt. Mater.*, 2021, **9**, 2002213.
5 B. Su, M. Li, E. Song and Z. Xia, Sb^{3+}-Doping in Cesium Zinc Halides Single Crystals Enabling High-Efficiency Near-Infrared Emission, *Adv. Funct. Mater.*, 2021, **31**, 2105316.

6 Y. Dong, Y. Han, R. Chen, Y. Lin and B.-B. Cui, Recent Progress of Triplet State Emission in Organic-Inorganic Hybrid Metal Halides, *J. Lumin.*, 2022, **249**, 119013.
7 T. Chen, Y. J. Ma and D. Yan, Single-Component 0D Metal–Organic Halides with Color-Variable Long-Afterglow toward Multi-Level Information Security and White-Light LED, *Adv. Funct. Mater.*, 2023, **33**, 2214962.
8 D. Chen, S. Hao, G. Zhou, C. Deng, Q. Liu, S. Ma, C. Wolverton, J. Zhao and Z. Xia, Lead-Free Broadband Orange-Emitting Zero-Dimensional Hybrid $(PMA)_3InBr_6$ with Direct Band Gap, *Inorg. Chem.*, 2019, **58**, 15602–15609.
9 J. Shamsi, A. S. Urban, M. Imran, L. De Trizio and L. Manna, Metal Halide Perovskite Nanocrystals: Synthesis, Post-Synthesis Modifications, and Their Optical Properties, *Chem. Rev.*, 2019, **119**, 3296–3348.
10 L. Zheng, X. Li, X. Lian, R. Xu, X. Liu, T. Xuan, R. Zeng, W. X. Ni and B. Luo, Weakening Ligand-Liquid Affinity to Suppress the Desorption of Surface-Passivated Ligands from Perovskite Nanocrystals, *Langmuir*, 2022, **38**, 15747–15755.
11 J. Wu, X. Li, X. Lian, B. Su, J. Pang, M. D. Li, Z. Xia, J. Z. Zhang, B. Luo and X. C. Huang, Ultrafast Study of Exciton Transfer in Sb(III)-Doped Two-Dimensional $[NH_3(CH_2)_4NH_3]CdBr_4$ Perovskite, *ACS Nano*, 2021, **15**, 15354–15361.
12 B. Luo, Y. Guo, Y. Xiao, X. Lian, T. Tan, D. Liang, X. Li and X. Huang, Fluorinated Spacers Regulate the Emission and Bandgap of Two-Dimensional Single-Layered Lead Bromide Perovskites by Hydrogen Bonding, *J. Phys. Chem. Lett.*, 2019, **10**, 5271–5276.
13 B. Luo, D. Liang, S. Sun, Y. Xiao, X. Lian, X. Li, M. D. Li, X. C. Huang and J. Z. Zhang, Breaking Forbidden Transitions for Emission of Self-Trapped Excitons in Two Dimensional $(F_2CHCH_2NH_3)_2CdBr_4$ Perovskite through Pb Alloying, *J. Phys. Chem. Lett.*, 2020, **11**, 199–205.
14 X. Li, X. Lian, J. Pang, B. Luo, Y. Xiao, M. D. Li, X. C. Huang and J. Z. Zhang, Defect-Related Broadband Emission in Two-Dimensional Lead Bromide Perovskite Microsheets, *J. Phys. Chem. Lett.*, 2020, **11**, 8157–8163.
15 C. He, J. Qiu, Z. Mu and X. Liu, Unlocking the Potential of Halide Perovskites Through Doping, *CCS Chem.*, 2023, **5**, 1961–1972.
16 C. Chen, S. Zhang, R. Zeng, B. Luo, Y. Chen, S. Cao, J. Zhao, B. Zou and J. Z. Zhang, Competing Energy Transfer in Two-Dimensional Mn^{2+}-Doped $BDACdBr_4$ Hybrid Layered Perovskites with Near-Unity Photoluminescence Quantum Yield, *ACS Appl. Mater. Interfaces*, 2022, **14**, 45725–45733.
17 Y. Chen, R. Zeng, Q. Wei, S. Zhang, B. Luo, C. Chen, X. Zhu, S. Cao, B. Zou and J. Z. Zhang, Competing Energy Transfer-Modulated Dual Emission in Mn^{2+}-Doped $Cs_2NaTbCl_6$ Rare-Earth Double Perovskites, *J. Phys. Chem. Lett.*, 2022, **13**, 8529–8536.
18 L. Li, W. Wu, D. Li, C. Ji, S. Lin, M. Hong and J. Luo, Highly Efficient White-Light Emission Induced by Carboxylic Acid Dimers in a Layered Hybrid Perovskite, *CCS Chem.*, 2022, **4**, 2491–2497.
19 W. Ma, Q. Qian, S. M. H. Qaid, S. Zhao, D. Liang, W. Cai and Z. Zang, Water-Molecule-Induced Reversible Fluorescence in a One-Dimensional Mn-Based Hybrid Halide for Anticounterfeiting and Digital Encryption-Decryption, *Nano Lett.*, 2023, **23**, 8932–8939.
20 X. Li, C. Peng, Y. Xiao, D. Xue, B. Luo and X.-C. Huang, Guest-Induced Reversible Phase Transformation of Organic–Inorganic Phenylpiperazinium Antimony(III) Chlorides with Solvatochromic Photoluminescence, *J. Phys. Chem. C*, 2021, **125**, 25112–25118.
21 S. Zhou, Y. Chen, K. Li, X. Liu, T. Zhang, W. Shen, M. Li, L. Zhou and R. He, Photophysical Studies for Cu(I)-Based Halides: Broad Excitation Bands and Highly Efficient Single-Component Warm White-Light-Emitting Diodes, *Chem. Sci.*, 2023, **14**, 5415–5424.
22 Z. Li, Y. Li, P. Liang, T. Zhou, L. Wang and R.-J. Xie, Dual-Band Luminescent Lead-Free Antimony Chloride Halides with Near-Unity Photoluminescence Quantum Efficiency, *Chem. Mater.*, 2019, **31**, 9363–9371.
23 B. Su, G. Song, M. S. Molokeev, N. N. Golovnev, M. K. Lesnikov, Z. Lin and Z. Xia, Role of Metal-Chloride Anions in Photoluminescence Regulations for Hybrid Metal Halides, *J. Phys. Chem. Lett.*, 2021, **12**, 1918–1925.
24 Y. Wu, C.-M. Shi, S.-R. Kang and L.-J. Xu, Antimony-Doped Indium-Based Halide Single Crystals Enabling White-Light Emission, *Inorg. Chem. Front.*, 2022, **9**, 5008–5015.
25 Q. Ren, J. Zhang, M. S. Molokeev, G. Zhou and X.-M. Zhang, Triplet–Triplet Energy Transfer from Bi^{3+} to Sb^{3+} in Zero-Dimensional Indium Hybrids via a B-Site Co-doping Strategy toward White-Light Emission, *Inorg. Chem. Front.*, 2022, **9**, 5960–5968.
26 Y. Jing, Y. Liu, X. Jiang, M. S. Molokeev, Z. Lin and Z. Xia, Sb^{3+} Dopant and Halogen Substitution Triggered Highly Efficient and Tunable Emission in Lead-Free Metal Halide Single Crystals, *Chem. Mater.*, 2020, **32**, 5327–5334.
27 J. Zhou, M. Li, M. S. Molokeev, J. Sun, D. Xu and Z. Xia, Tunable Photoluminescence in Sb^{3+}-Doped Zero-Dimensional Hybrid Metal Halides with Intrinsic and Extrinsic Self-Trapped Excitons, *J. Mater. Chem. C*, 2020, **8**, 5058–5063.
28 C. Fang, Y. Mao, G. Zhou, Z. Zhang, Y. Zhu, D. Xu, X. Li, A. Geng and J. Zhou, Zero-Dimensional Indium Hybrids and Modulated Photoluminescence by Sb Doping, *Mater. Chem. Front.*, 2023, **7**, 3164.
29 X. Liu, X. Xu, B. Li, Y. Liang, Q. Li, H. Jiang and D. Xu, Antimony-Doping Induced Highly Efficient Warm-White Emission in Indium-Based Zero-Dimensional Perovskites, *CCS Chem.*, 2020, **2**, 216–224.
30 K. Liu, S. Hao, J. Cao, J. Lin, L. Fan, X. Zhang, Z. Guo, C. Wolverton, J. Zhao and Q. Liu, Antimony doping to enhance luminescence of tin(IV)-based hybrid metal halides, *Inorg. Chem. Front.*, 2022, **9**, 3865–3873.
31 Z. Wu, J. Nitsch and T. B. Marder, Persistent Room-Temperature Phosphorescence from Purely Organic Molecules and Multi-Component Systems, *Adv. Opt. Mater.*, 2021, **9**, 2100411.

32 X. Liu, X. Li, J. Li, X. Lian, Y. Xiao, R. Zeng, S.-F. Ni, K. Xu, Y. Kuai, W.-X. Ni and B. Luo, Modulating Anthracene Excimer through Guest Engineering in Two-Dimensional Lead Bromide Hybrids, *Inorg. Chem. Front.*, 2023, **10**, 2917–2925.

33 S. Feng, Y. Ma, S. Wang, S. Gao, Q. Huang, H. Zhen, D. Yan, Q. Ling and Z. Lin, Light/Force-Sensitive 0D Lead-Free Perovskites: From Highly Efficient Blue Afterglow to White Phosphorescence with Near-Unity Quantum Efficiency, *Angew. Chem., Int. Ed.*, 2022, **61**, e202116511.

34 C. Xing, B. Zhou, D. Yan and W.-H. Fang, Dynamic Photoresponsive Ultralong Phosphorescence from One-Dimensional Halide Microrods Toward Multilevel Information Storage, *CCS Chem.*, 2023, 1–11, DOI: 10.31635/ccschem.023.202202605.

35 L. J. Xu, A. Plaviak, X. Lin, M. Worku, Q. He, M. Chaaban, B. J. Kim and B. Ma, Metal Halide Regulated Photophysical Tuning of Zero-Dimensional Organic Metal Halide Hybrids: From Efficient Phosphorescence to Ultralong Afterglow, *Angew. Chem., Int. Ed.*, 2020, **59**, 23067–23071.

36 J. H. Wei, W. T. Ou, J. B. Luo and D. B. Kuang, Zero-Dimensional Zn-Based Halides with Ultra-Long Room-Temperature Phosphorescence for Time-Resolved Anti-Counterfeiting, *Angew. Chem., Int. Ed.*, 2022, **61**, e202207985.

37 M. Chaaban, A. Ben-Akacha, M. Worku, S. Lee, J. Neu, X. Lin, J. S. R. Vellore Winfred, C. J. Delzer, J. P. Hayward, M. H. Du, T. Siegrist and B. Ma, Metal Halide Scaffolded Assemblies of Organic Molecules with Enhanced Emission and Room Temperature Phosphorescence, *J. Phys. Chem. Lett.*, 2021, **12**, 8229–8236.

38 Z. Li, M. Cao, Z. Rao, X. Zhao and X. Gong, Tunable Afterglow and Self-Trapped Exciton Emissions in Zr(IV)-Based Organic-Inorganic Metal Halide Hybrids by Metal-Ion Doping, *Small*, 2023, **19**, 2302357.

39 S. Yang, B. Zhou, Q. Huang, S. Wang, H. Zhen, D. Yan, Z. Lin and Q. Ling, Highly Efficient Organic Afterglow from a 2D Layered Lead-Free Metal Halide in Both Crystals and Thin Films under an Air Atmosphere, *ACS Appl. Mater. Interfaces*, 2020, **12**, 1419–1426.

40 Z. Luo, Y. Liu, Y. Liu, C. Li, Y. Li, Q. Li, Y. Wei, L. Zhang, B. Xu, X. Chang and Z. Quan, Integrated Afterglow and Self-Trapped Exciton Emissions in Hybrid Metal Halides for Anti-Counterfeiting Applications, *Adv. Mater.*, 2022, **34**, e2200607.

41 P. Zhou and K. Han, Unraveling the Detailed Mechanism of Excited-State Proton Transfer, *Acc. Chem. Res.*, 2018, **51**, 1681–1690.

42 W.-S. Yu, C.-C. Cheng, Y.-M. Cheng, P.-C. Wu, Y.-H. Song, Y. Chi and P.-T. Chou, Excited-State Intramolecular Proton Transfer in Five-Membered Hydrogen-Bonding Systems: 2-Pyridyl Pyrazoles, *J. Am. Chem. Soc.*, 2003, **125**, 10800–10801.

43 L. Bian, H. Ma, W. Ye, A. Lv, H. Wang, W. Jia, L. Gu, H. Shi, Z. An and W. Huang, Color-Tunable Ultralong Organic Phosphorescence Materials for Visual UV-Light Detection, *Sci. China: Chem.*, 2020, **63**, 1443–1448.

44 G. Song, M. Li, S. Zhang, N. Wang, P. Gong, Z. Xia and Z. Lin, Enhancing Photoluminescence Quantum Yield in 0D Metal Halides by Introducing Water Molecules, *Adv. Funct. Mater.*, 2020, **30**, 2002468.

45 H. Arfin, A. S. Kshirsagar, J. Kaur, B. Mondal, Z. Xia, S. Chakraborty and A. Nag, ns^2 Electron (Bi^{3+} and Sb^{3+}) Doping in Lead-Free Metal Halide Perovskite Derivatives, *Chem. Mater.*, 2020, **32**, 10255–10267.

46 Y. Zhang, X. Liu, H. Sun, J. Zhang, X. Gao, C. Yang, Q. Li, H. Jiang, J. Wang and D. Xu, Strong Self-Trapped Exciton Emissions in Two-Dimensional Na-In Halide Perovskites Triggered by Antimony Doping, *Angew. Chem., Int. Ed.*, 2021, **60**, 7587–7592.

47 S. He, X. Luo, X. Liu, Y. Li and K. Wu, Visible-to-Ultraviolet Upconversion Efficiency above 10% Sensitized by Quantum-Confined Perovskite Nanocrystals, *J. Phys. Chem. Lett.*, 2019, **10**, 5036–5040.